Modeling of Supercritical Oxidation of Aqueous Wastes in a Deep-Well Reactor

Dusan Kodra and Vemuri Balakotaiah
Dept. of Chemical Engineering, University of Houston, Houston, TX 77204

A mathematical model is developed for deep-well oxidation of wastes in supercritical water. The model accounts for the variation of thermodynamic and transport properties with temperature and pressure. It is used to examine the steady-state behavior of the supercritical-water deep-well oxidation reactors. The effects of inlet flow rate, heat losses from the reactor, inlet concentration of organics, oxygen injection depth, reactor length, inlet pressure, and inlet temperature on the exit conversion and the bottom temperature are examined. The simulations show that under practical conditions the capacity of the reactor is dictated by hydrodynamic considerations rather than the oxidation kinetics, and that obtaining temperatures of 10 to 50 K above critical temperature at the bottom of the reactor requires longer tubes and/or high inlet pressures. Heat losses to the earth can be modeled accurately by treating the earth as an infinite reservoir by properly choosing the effective heat-transfer coefficient.

Introduction

Wet-air oxidation is a well known process used for the treatment of waste water. At elevated temperature and pressure (around 475 K and 12.5 MPa) and in the presence of oxygen, the chemical oxygen demand (COD) removal of up to 80% can be achieved in this process. It is the basis for the Zimpro process that has been used successfully in the U.S. and Europe since the early 1960s for the conditioning and oxidation of municipal sludge. Operating costs of the Zimpro process are very favorable compared to incineration for waste waters with low concentrations of organics. The reason is that the oxidation is carried out directly in waste water and no additional energy is required for evaporation of the water. Slow oxidation kinetics, however, lead to longer residence times to achieve the required COD removal. In addition, high-pressure vessels, pumps and compressors are needed that result in high capital costs for the Zimpro process. There are also safety concerns associated with the above-the-ground process. An alternative to the above-the-ground process is the deep-well reactor configuration that consists of concentric tubes of length between 1,400 and 3,000 m inserted in a conventionally drilled and cased well in the earth (Figure 1). Some advantages of the deep-well configuration are: minimizing material requirements by taking advantage of the balance between earth pressure outside and reactor pressure in the interior, achieving the desired high pressure in the reaction zone at the bottom of the reactor by hydrostatic head, large surface area for countercurrent heat exchange between descending reactants and ascending products, and the insulating properties of the earth that minimize heat losses from the reactor. The technical feasibility of the deep-well process was demonstrated by building an EPA-sponsored full-scale deep-well wet oxidation reactor in Longmont, Colorado, which became operational in June 1983. The reactor was 1,520-m-long and was designed to process 5,600 kg of COD per day utilizing air as the oxidizing medium. However, an oxygen enrichment capability added to the system in September 1984 has more than tripled the system capacity by allowing an increase in the COD feed concentrations from 10,000 to 36,000 mg/L (Rappe and Schwayer, 1985). Downhole temperatures from 260 to 288°C and pressures from 9.0 to 12.4 MPa allowed COD reductions of greater than 75% under normal process conditions (Kaufmann and Peterschek, 1986).

Much higher destruction efficiency can be obtained if the operating temperature and pressure are raised above critical values for water (373.976°C and 22.055 MPa). Modell et al. (1982) demonstrated the high destruction efficiency of super-

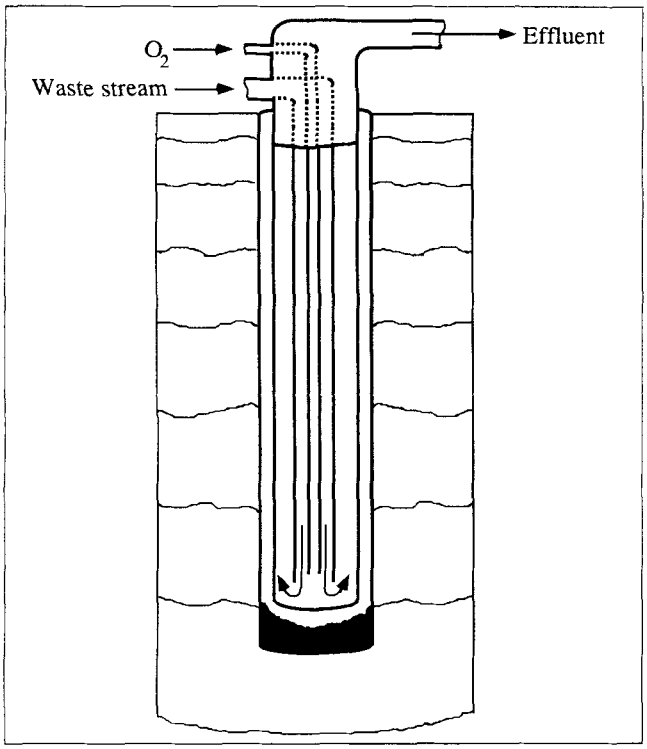

Figure 1. Deep-well oxidation reactor.

critical water oxidation. Various model compounds were used including many chlorinated hydrocarbons such as DDT, PCB 1234, PCB 1254 and 4,4′-dichlorobiphenyl. The efficiency for organic chloride destruction exceeded 99.99%, and the destruction efficiency for total organic carbon was over 99.97%. Thomason and Modell (1984) report that in a series of experiments using various nitrogen-containing compounds, the total organic carbon destruction efficiency was over 99.99% at a temperature of 574°C.

The main reason for supercritical water being considered an ideal medium for treating hazardous wastes is that it behaves much as a moderately polar organic liquid does under ambient conditions (Thomason and Modell, 1984). Common organic nonpolar compounds, such as benzene and *n*-heptane that are hardly soluble in water under ambient conditions suddenly become miscible in all proportions with supercritical water. The same is true for oxygen as well as other gases. On the other hand, the solvatization and ionization power of supercritical water drop significantly, and lead to extremely low solubility of inorganic salts such as NaCl. Thus, supercritical water can be used to destroy wastes with oxygen in a homogeneous (one-phase) mixture, while changing the oxygen to waste concentration ratio in a broad range. Also, by addition of a base to the feed, the products of oxidation, which are in the form of acids, can be easily precipitated out as inorganic salts (Thomason and Modell, 1984).

There have already been some attempts to commercialize the supercritical oxidation processes. Modar Inc. was working on above-the-ground oxidation systems suitable for complete destruction of hazardous materials in a broad range of capacities (Thomason and Model, 1984; Josephson, 1982). Vertech Inc., which built and operated the Longmont's deep-well subcritical waste water treatment plant, analyzed possibilities of the supercritical deep-well process (Smith and Raptis, 1986). Their analysis shows that this technology is best suited for large-volume (0.4–4.0 m^3/min) dilute (1.0–10,000 mg/L COD) aqueous wastes. Destruction efficiencies of hazardous wastes equal to or greater than the EPA requirements (up to 99.9999%) could be met.

Shanableh and Gloyna (1990) have recently built several bench- and pilot-scale supercritical oxidation systems using batch and tubular flow reactors. Some of their tubular reactor systems are similar to the deep-well reactor configuration. Although these bench-scale experiments provide some useful insight into this technology, the results obtained cannot be used directly in scale-up of the deep-well reactor. The reason is that the same fluid is used in bench- and full-scale units, making it impossible to match all the dimensionless groups. The strong interaction between fluid flow, heat transfer, and chemical reaction makes scale-up based solely on lab- and pilot-plant-scale experiments practically impossible. Mathematical models of the process are necessary for an initial successful design of a commercial-scale reactor.

Some studies on the modeling and simulation of the deep-well process have also appeared in the literature. Kaufmann and Peterschek (1986) presented simulations of Longmont's deep-well reactor for the oxidation of municipal sludge. Tezduyar et al. (1987) and Mittal et al. (1991) analyzed the startup procedures of the deep-well reactor for the case of a constant heat source.

Lovo et al. (1990) presented steady-state results of modeling and simulation of the deep-well process for subcritical conditions. Lovo and Balakotaiah (1992a,b) addressed an important issue in the design and operation of deep-well reactors, that is, the autothermal operation and its effect on the ignition and extinction behavior of the reactor.

In this work, we develop and analyze a mathematical model of the deep-well process for operation under supercritical conditions. This model accounts for the variation of physical properties with temperature and pressure, as well as the variation of the heat-transfer coefficient between the tubes. The effect of the inlet flow rate, heat losses from the reactor, the inlet concentration of organics, oxygen injection depth, reactor length, inlet pressure and inlet temperature on the reactor performance is examined. Also, various methods for the estimation of heat losses from the reactor are compared.

Mathematical Model for Supercritical Operation

The temperature and pressure within the deep-well reactor vary in a broad range from ambient conditions to values above the critical point of water. Therefore, the variation in the thermodynamic and transport properties of the reaction mixture with temperature and pressure can be significant. In developing a mathematical model, we account for the variations in density, specific heat capacities, dynamic viscosity, and thermal conductivity. We assume that the properties of the reacting mixture can be approximated by the properties of pure water.

All the thermodynamic properties of water are calculated using an analytic expression for the Helmholtz function (specific Helmholtz energy) in the form:

$$\underline{A} = \underline{A}(\rho^*, T)$$

where $\underline{A}$ is the Helmholtz function, ρ^* is the density, and T is the absolute temperature (Haar et al., 1984). Because $\underline{A}(\rho^*, T)$ is everywhere a single-valued, analytic function, it is straightforward to evaluate the appropriate first and second derivatives needed to obtain the various thermodynamic properties. The values for the transport properties (thermal conductivity and dynamic viscosity) are estimated from experimentally obtained approximations of the dependence of these properties on density and temperature (Haar et al., 1984).

We assume that the pressure at the inlet and exit of the reactor is high enough that gases remain dissolved and one phase flow exists in both tubes. We also assume that the oxygen dissolves immediately after being injected into the waste-water stream. The reactions taking place are lumped together and approximated by a single irreversible reaction:

$$A + \nu B \rightarrow P$$

where A represents the organic component, B is oxygen, and P represents the products of reaction (water and various oxides). First-order dependence of the rate on the concentration of the organic component was reported in the literature for supercritical-water oxidation (Helling and Tester, 1987, 1988; Yang and Eckert, 1988; Webley and Tester, 1989). Thus, we assume that the rate is given by $r = k_o \exp(-E_{act}/RT)C_A$, where A (the organic component) is the limiting reactant.

The length to diameter ratio is extremely high ($\approx 15{,}000$) for supercritical deep-well reactors. Therefore, the process is convection-dominated, and mass-dispersion effects are clearly negligible. In addition, we assume that the heat conduction within each tube is negligible compared to the heat transfer between the tubes. The mass-flow rate of oxygen in the central tube as well as its heat capacity is assumed to be negligible compared to the mass-flow rate and the heat capacity of the downcoming reaction stream.

With these assumptions, we can write the following species and energy balances, continuity equations, and momentum balances for the down- and up-tube of the reactor.

Species balances:

$$\frac{\partial x_d}{\partial t} + v_d^* \frac{\partial x_d}{\partial z} + k_o \exp\left(-\frac{E_{act}}{RT_d}\right) x_d H(z - z_{in}) \hat{H}_d = 0 \qquad (1)$$

$$\frac{\partial x_u}{\partial t} - v_u^* \frac{\partial x_u}{\partial z} + k_o \exp\left(-\frac{E_{act}}{RT_u}\right) x_u \hat{H}_u = 0 \qquad (2)$$

Energy balances (for derivation of energy balances see Appendix A):

$$A_{md}\rho_m^* C_{vm}^* \frac{\partial T_d}{\partial t} + A_d \rho_d^* \hat{C}_{Pd}^* \frac{\partial T_d}{\partial t} + A_d \rho_d^* \hat{C}_{Td}^* \frac{\partial P_d}{\partial t}$$
$$+ A_d \rho_d^* v_d^* \hat{C}_{Pd}^* \frac{\partial T_d}{\partial z} + A_d \rho_d^* v_d^* \hat{C}_{Td}^* \frac{\partial P_d}{\partial z} + A_d \frac{\partial}{\partial z}(P_d^* v_d^*)$$
$$- A_d(-\Delta \underline{H}_r) k_o \exp\left(-\frac{E_{act}}{RT_d}\right) x_d \rho_d^* H(z - z_{in}) \hat{H}_d$$
$$- p_d U_d^* (T_u - T_d) = 0 \qquad (3)$$

$$A_{mu}\rho_m^* C_{vm}^* \frac{\partial T_u}{\partial t} + A_u \rho_u^* \hat{C}_{Pu}^* \frac{\partial T_u}{\partial t} + A_u \rho_u^* \hat{C}_{Tu}^* \frac{\partial P_u}{\partial t}$$
$$- A_u \rho_u^* v_u^* \hat{C}_{Pu}^* \frac{\partial T_u}{\partial z} - A_u \rho_u^* v_u^* \hat{C}_{Tu}^* \frac{\partial P_u}{\partial z} - A_u \frac{\partial}{\partial z}(P_u^* v_u^*)$$
$$- A_u(-\Delta \underline{H}_r) k_o \exp\left(-\frac{E_{act}}{RT_u}\right) x_u \rho_u^* \hat{H}_u$$
$$+ p_d U_d^* (T_u - T_d) + Q_{loss} = 0 \qquad (4)$$

where

$$z_f(t) = z_{in} + \int_0^t v_f^* \, dt'$$

and

$$\left.\begin{aligned} \hat{H}_d &= 1 - H(z - z_f) \\ \hat{H}_u &= 0 \\ v_f^* &= v_d^*(z_f) \end{aligned}\right\} z_{in} < z_f \le L$$

$$\left.\begin{aligned} \hat{H}_d &= 1 \\ \hat{H}_u &= H[z - (2L - z_f)] \\ v_f^* &= v_u^*(2L - z_f) \end{aligned}\right\} L < z_f < 2L$$

$$\left.\begin{aligned} \hat{H}_d &= 1 \\ \hat{H}_u &= 1 \end{aligned}\right\} z_f \ge 2L \qquad (5)$$

Continuity equations:

$$\frac{\partial \rho_d^*}{\partial t} + \frac{\partial (v_d^* \rho_d^*)}{\partial z} = 0 \qquad (6)$$

$$\frac{\partial \rho_u^*}{\partial t} - \frac{\partial (v_u^* \rho_u^*)}{\partial z} = 0 \qquad (7)$$

Momentum balances:

$$\rho_d^* \frac{\partial v_d^*}{\partial t} + \rho_d^* v_d^* \frac{\partial v_d^*}{\partial z} + \frac{\partial P_d^*}{\partial z} + f_d \frac{v_d^{*2} \rho_d^*}{8 R_{hd}} - \rho_d^* g = 0 \qquad (8)$$

$$\rho_u^* \frac{\partial v_u^*}{\partial t} - \rho_u^* v_u^* \frac{\partial v_u^*}{\partial z} - \frac{\partial P_u^*}{\partial z} + f_u \frac{v_u^{*2} \rho_u^*}{8 R_{hu}} + \rho_u^* g = 0 \qquad (9)$$

We have introduced Heaviside's function H in the species and energy balances for the down-tube. Its role is to make the reaction term equal to zero for $z \le z_{in}$, that is for the region above the point where oxygen is injected into the waste-water stream flowing downward. The second function, denoted by $\hat{H}_i$ $(i = d,u)$, appears in the equations for the down- as well as up-tubes and is introduced instead of the species balance for oxygen. It makes the reaction term at a certain point along the reactor zero until the reaction front, which is at $z = z_{in}$ for $t = 0$ and at $z = z_f(t)$ for $t > 0$, reaches this point. In other words, although the oxygen concentration does not appear in the rate expression, the reaction term is zero at a certain point until the waste-water stream containing oxygen reaches this point.

For steady-state simulations, the value of $\hat{H}_i$ equals unity.

The friction factor, f_i, in the down- and up-tube is estimated by the following equation (Haaland, 1983):

$$\frac{1}{\sqrt{f_i}} = -1.8 \log\left[\frac{6.9}{Re_i} + \left(\frac{e_i}{14.8R_{hi}}\right)^{1.11}\right] \tag{10}$$

where $i = d,u$.

The heat-transfer coefficient at the inner surface of the down-tube can be estimated by using the well-known Dittus-Boelter equation (Eq. 11), provided that an equivalent diameter, which equals four times the hydraulic radius of the annulus, is used (Monrad and Pelton, 1942). A little modified equation (Eq. 12) is suggested for the heat-transfer coefficient at the outer surface of the down-tube (Monrad and Pelton, 1942):

$$Nu_d = 0.023 Re_d^{0.8} Pr_d^{0.4} \tag{11}$$

$$Nu_u = 0.02 Re_u^{0.8} Pr_u^{0.3} \left(\frac{D_u}{D_d}\right)^{0.53} \tag{12}$$

Thermodynamic and transport properties are estimated using codes published by Haar et al. (1984). Equations 1-4 and 6-9 are subject to the following initial and boundary conditions:

$$\begin{aligned}
&\text{At } t=0, \quad \forall z: && x_i = x_i(0,z)\\
& && T_i = T_i(0,z)\\
& && v_i^* = v_i^*(0,z)\\
& && P_i^* = P_i^*(0,z) \qquad (i = u,d)\\
&\text{At } z=0, \quad t>0: && x_d = x_o\\
& && T_d = T_o\\
& && v_d^* = v_o\\
& && P_d^* = P_o\\
&\text{At } z=L, \quad t>0: && x_u = x_d\\
& && T_u = T_d\\
& && v_u^* A_u = v_d^* A_d\\
& && P_u^* = P_d^*
\end{aligned} \tag{13}$$

The term Q_{loss} in Eq. 4 represents the heat loss per unit length of the up-tube from the reactor to the surrounding earth. This loss can be determined by simultaneously solving the unsteady-state conduction equation for the earth and the reactor equations. This approach, however, has some disadvantages, especially for steady-state calculations. Namely, the flux at the surface of the reactor estimated by solving the unsteady-state conduction equations for the earth changes with time even for very large times. It also depends on the temperature history of the up-tube. In addition, the approach used by Lovo et al. (1990) for estimation of heat losses is favorable from a computational point of view. Therefore, we model the heat losses to the surrounding strata in a way similar to that of Lovo et al. (1990)

$$Q_{\text{loss}} = p_u U_u^* (T_d - T_e) \tag{14}$$

where T_e is the temperature of the earth at a depth z given by:

$$T_e = T_a + \alpha z \tag{15}$$

where α is the natural temperature gradient ($= 0.029\ \text{K}\cdot\text{m}^{-1}$).

The value of the heat-transfer coefficient, U_u^*, strongly affects the amount of heat lost from the reactor and consequently the reactor behavior. In Appendix B, we illustrate the method used to estimate the value of the heat-transfer coefficient, U_u^*. The value $U_u^* = 2.0\ \text{W}\cdot\text{m}^{-2}\cdot\text{K}^{-1}$ has been chosen as a base value in our computations. This is well below the value $U_u^* = 5.7\ \text{W}\cdot\text{m}^{-2}\cdot\text{K}^{-1}$ used by Lovo et al. (1990).

Dimensionless Form of Equations

Equations 1-9 and 13-15 can be written in dimensionless form by defining the following dimensionless variables:

$$\begin{aligned}
&\zeta = \frac{z}{L} && \tau = \frac{t v_o^*}{L} && y_i = \frac{T - T_o}{T_o}\\
&v_i = \frac{v_i^*}{v_o^*} && \rho_i = \frac{\rho_i^*}{\rho_o^*} && X_i = \frac{x_o - x_i}{x_o}\\
&P_i = \frac{P_i^*}{P_o^*} && Ri = \frac{g^* L}{v_o^{*2}} && \beta = \frac{x_o(-\Delta H_r)}{C_{vo}^* T_o}\\
&\gamma = \frac{E_{\text{act}}}{RT_o} && \epsilon_i = \frac{A_{mi}\rho_{mi}^* C_{vm}^*}{A_i \rho_o^* C_{vo}^*} && a = \frac{A_u}{A_d}\\
&Da = \frac{Lk(T_o)}{v_o^*} && St = \frac{p_d U_{do}^* L}{v_o^* A_d \rho_o^* C_{vo}^*} && St_e = \frac{p_u U_u^* L}{v_o^* A_d \rho_o^* C_{vo}^*}\\
&\Omega = \frac{P_o^*}{T_o \rho_o^* C_{vo}^*} && Eu = \frac{P_o^*}{\rho_o^* v_o^2} && b_i = \frac{L}{8R_{hi}}\\
&U_d = \frac{U_d^*}{U_{do}^*} && \hat{C}_{Pi} = \frac{\hat{C}_{Pi}^*}{C_{vo}^*} && \hat{C}_{Ti} = \frac{P_o^* \hat{C}_{Ti}^*}{T_o C_{vo}^*}
\end{aligned} \qquad (i = d,u) \tag{16}$$

After substitution of these into Eqs. 1-13, we obtain the following set of equations:

$$\frac{\partial X_d}{\partial \tau} + v_d \frac{\partial X_d}{\partial \zeta} - Da \exp\left\{\frac{\gamma y_d}{1 + y_d}\right\}(1 - X_d) H(\zeta - \zeta_{in}) \hat{H}_d = 0 \tag{17}$$

$$\frac{\partial X_u}{\partial \tau} - v_u \frac{\partial X_u}{\partial \zeta} - Da \exp\left\{\frac{\gamma y_u}{1 + y_u}\right\}(1 - X_u) \hat{H}_u = 0 \tag{18}$$

$$\begin{aligned}
&(\epsilon_d + \rho_d \hat{C}_{Pd}) \frac{\partial y_d}{\partial \tau} + \rho_d \hat{C}_{Td} \frac{\partial P_d}{\partial \tau} + \rho_d v_d \left(\hat{C}_{Pd} \frac{\partial y_d}{\partial \zeta} + \hat{C}_{Td} \frac{\partial P_d}{\partial \zeta}\right)\\
&\quad + \Omega \frac{\partial (P_d v_d)}{\partial \zeta} - Da \beta \rho_d \exp\left\{\frac{\gamma y_d}{1 + y_d}\right\}(1 - X_d) H(\zeta - \zeta_{in}) \hat{H}_d\\
&\quad - St U_d (y_u - y_d) = 0
\end{aligned} \tag{19}$$

$$(\epsilon_u + a\rho_u \hat{C}_{Pu}) \frac{\partial y_u}{\partial \tau} + a\rho_u \hat{C}_{Tu} \frac{\partial P_u}{\partial \tau} - a\rho_u v_u \left(\hat{C}_{Pu} \frac{\partial y_u}{\partial \zeta} + \hat{C}_{Tu} \frac{\partial P_u}{\partial \zeta}\right)$$

$$-a\Omega\frac{\partial(P_u v_u)}{\partial\zeta}-aDa\beta\rho_u\exp\left\{\frac{\gamma y_u}{1+y_u}\right\}(1-X_u)\hat{H}_i$$
$$+StU_d(y_u-y_d)+St_e(y_u-y_e)=0 \quad (20)$$

where

$$\zeta_f(\tau)=\xi_{in}+\int_0^\tau v_f d\tau'$$

and

$$\left.\begin{aligned}\hat{H}_d&=1-H(\zeta-\zeta_f)\\ \hat{H}_u&=0\\ v_f&=v_d(\zeta_f)\end{aligned}\right\}\ \zeta_{in}<\zeta_f\le 1$$

$$\left.\begin{aligned}\hat{H}_d&=1\\ \hat{H}_u&=H[\zeta-(2-\zeta_f)]\\ v_f&=v_u(2-\zeta_f)\end{aligned}\right\}\ 1<\zeta_f<2$$

$$\left.\begin{aligned}\hat{H}_d&=1\\ \hat{H}_u&=1\end{aligned}\right\}\ \zeta_f\ge 2 \quad (21)$$

$$\frac{\partial\rho_d}{\partial\tau}+\frac{\partial(v_d\rho_d)}{\partial\zeta}=0 \quad (22)$$

$$\frac{\partial\rho_u}{\partial\tau}-\frac{\partial(v_u\rho_u)}{\partial\zeta}=0 \quad (23)$$

$$\rho_d\frac{\partial v_d}{\partial\tau}+\rho_d v_d\frac{\partial v_d}{\partial\zeta}+Eu\frac{\partial P_d}{\partial\zeta}+f_d v_d^2\rho_d b_d-Ri\rho_d=0 \quad (24)$$

$$\rho_u\frac{\partial v_u}{\partial\tau}-\rho_u v_u\frac{\partial v_u}{\partial\zeta}-Eu\frac{\partial P_u}{\partial\zeta}+f_u v_u^2\rho_u b_u+Ri\rho_u=0 \quad (25)$$

The initial and boundary conditions take the following form:

At $\tau=0$, $0\le\zeta\le 1$
$X_i=X_i(0,\zeta)$
$y_i=y_i(0,\zeta)$
$v_i=v_i(0,\zeta)$
$P_i=P_i(0,\zeta)$ $(i=u,d)$

At $\zeta=0$, $\tau>0$
$X_d=0$
$y_d=0$
$v_d=1$
$P_d=1$

At $\zeta=1$, $\tau>0$
$X_u=X_d$
$y_u=y_d$
$av_u=v_d$
$P_u=P_d$ (26)

The above model equations are written in a form similar to that used by Lovo et al. (1990) to describe the subcritical deep-well oxidation process. The dependence of the reaction stream properties on temperature and pressure, however, requires introduction of some additional quantities. While the definition of dimensionless density ρ_i, velocity v_i, and overall heat-transfer coefficient (U_d) between the up- and down-tubes is straightforward, the introduction of the dimensionless partial derivatives of internal energy with respect to temperature ($\hat{C}_P$) and pressure ($\hat{C}_T$) requires some additional explanation (for details, see Appendix A).

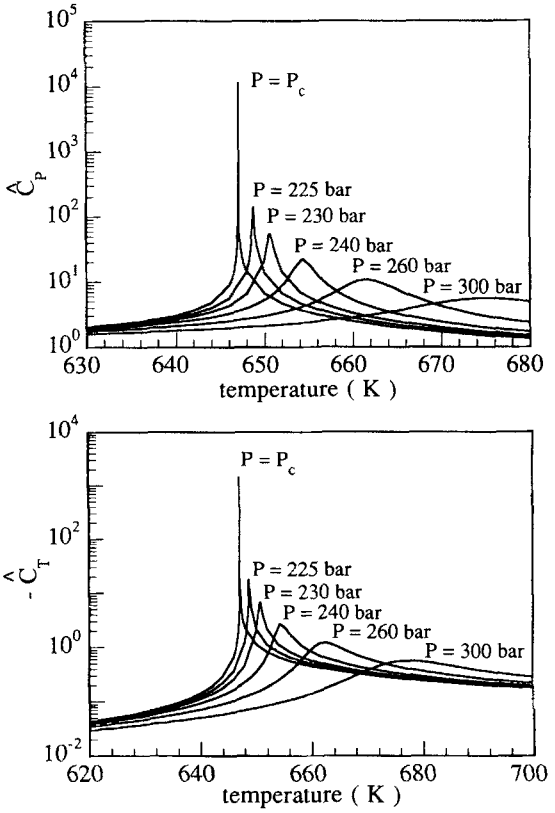

Figure 2. $\hat{C}_P$ and $\hat{C}_T$ vs. temperature for pressures above the critical pressure.

Figure 2 shows the values of $\hat{C}_P$ and $\hat{C}_T$ close to the critical point. For pressures greater than or equal to P_c, the plots of $\hat{C}_P$ and $\hat{C}_T$ vs. temperature exhibit a maximum whose value depends on the pressure. The peak value is the highest at the critical point and decreases rapidly as the pressure becomes higher. The loci of maxima are shown in Figure 3. The value of $\hat{C}_T$ is approximately one order of magnitude smaller than

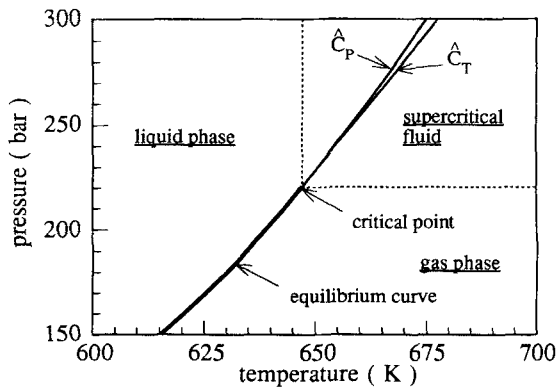

Figure 3. Loci of maximum values of $\hat{C}_P$ and $\hat{C}_T$ in the P-T plane.

Table 1. Fixed Parameter Values Used in the Simulation of the Deep-Well Reactor

A_d	(m^2)	0.0264
A_u	(m^2)	0.0292
k_o	(s^{-1})	1.0×10^5
E_{act}	($kJ\cdot mol^{-1}$)	74.36*
$(-\Delta H_r)$	($kJ\cdot kg^{-1}$)	1.0×10^4
e	(mm)	0.05

* $\gamma = 30.0$ at $T_o = 298.15$ K.

that of $\hat{C}_P$. The behavior of $\hat{C}_P$ influences strongly the performance of the supercritical oxidation process. The integral:

$$\int_T^{T+\Delta T} \hat{C}_P^* dT' \tag{27}$$

represents the change in the internal energy of reaction stream due an increase in the temperature by ΔT (while keeping pressure constant). This suggests that the amount of energy required to raise the temperature of the reaction stream above that corresponding to the locus of maximal $\hat{C}_P$ is large, if the pressure is only slightly above the critical value. Crossing the locus is much easier at pressures well above the critical value. As will be shown later, this phenomenon has a strong influence on the behavior of the supercritical deep-well oxidation process, since obtaining temperatures above 700 K at the bottom of the reactor (oxygen injection point) requires bottom pressures well above the critical value.

Steady-State Solution

The steady-state model may be obtained from Eqs. 17-26 by deleting the terms involving the time derivative. The model involves dimensionless parameters whose actual values depend on the design and operating conditions, the thermodynamic properties of the reaction stream, and kinetic data. Here, we analyze the steady-state behavior of the deep-well process by choosing a base case and then varying a distinguished parameter to obtain the impact of that parameter on the reactor performance (exit conversion and bottom temperature). We show the dependence of the reactor performance on the inlet velocity of the reaction stream, v_o^*; the inlet temperature, T_o; the reactor length, L; inlet pressure P_o^*; the heat-transfer coefficient from the up-tube to the surrounding earth, U_u^*; the weight fraction of organics in the feed, x_o; and the oxygen injection depth, ζ_{in}. Table 1 gives the values of the parameters that are fixed in the simulations. Table 2 shows the parameters that are varied and the range of variation.

Table 2. Range of Parameter Values Used in the Simulation of the Deep-Well Reactor

		Range	Base Case
v_o^*	($m\cdot s^{-1}$)	0.01 ... 3.0	1.0
T_o	(K)	280.0 ... 550.0	298.15
P_o^*	(MPa)	0.1 ... 25.0	10.0
L	(m)	1,500 ... 3,600	3,000
U_u^*	($W\cdot m^{-2}\cdot K^{-1}$)	0.0 ... 20.0	2.0
x_o	(wt. fraction)	0.0 ... 0.05	0.01
ζ_{in}	—	0.0 ... 1.0	1.0
C_{vo}^*	$J\cdot kg^{-1}\cdot K^{-1}$	—	4,106.4

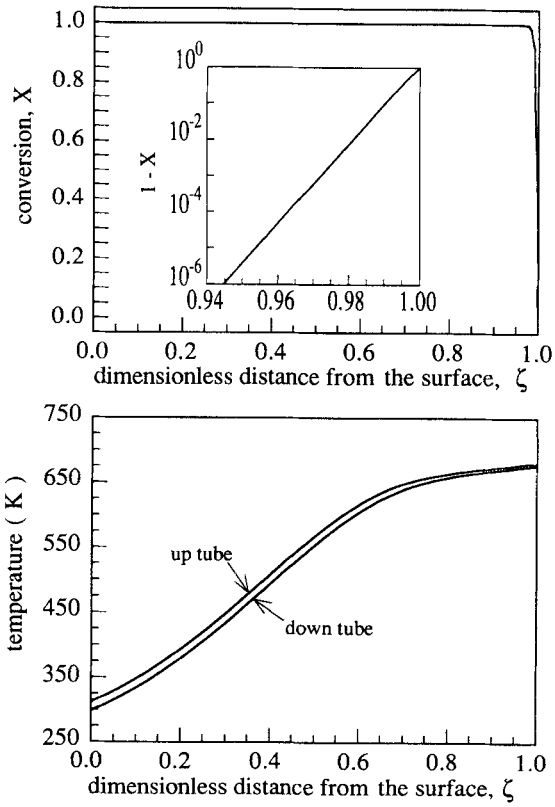

Figure 4. Conversion and temperature profiles of the ignited steady state for the base case.

Parameter values used to construct this figure are given in Tables 1 and 2.

First, we show various profiles within the reactor for the base case. Figure 4 shows the conversion and temperature profiles of the ignited steady state for the base case. The reaction is nearly completed within a short distance following the oxygen injection point at the bottom of the reactor. The inset shows that within the bottom 6% of the reactor more than 99.9999% of the organic component is oxidized. This fast destruction is caused by the very high temperature in this zone, as seen from the temperature profile. The feed reaching the bottom of the reactor is preheated by the countercurrent heat exchange between the up- and down-tubes to 677 K before it starts to react with the oxygen.

Figure 5 shows the pressure and density profiles within the reactor. Both Figures 4 and 5 show that the transition from the subcritical to the supercritical conditions in the down-tube occurs at $\zeta \approx 0.74$. Figure 5 also shows that the pressure in the up-tube is almost equal to that in the down-tube. The friction loss is counterbalanced by the buoyancy force due to the density difference between the down- and up-tubes, and the outlet pressure is slightly higher than the inlet pressure.

Figure 4 shows that the temperature in the up-tube is only slightly higher than that in the down-tube. This is due to the extremely efficient heat exchange between the tubes. The overall heat-transfer coefficient U_d^* varies within the reactor as shown in Figure 6. There is a maximum close to the point where the transition from subcritical to supercritical conditions occurs. This corresponds to the maximum in the value of specific heat at the constant pressure C_p^*. Although not shown

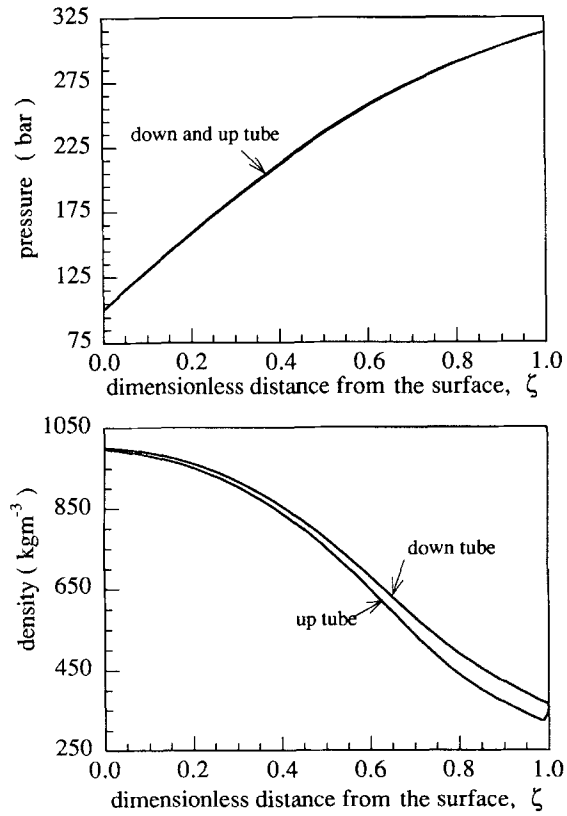

Figure 5. Pressure and density profiles of the ignited steady state for the base case.

Parameter values used to construct this figure are given in Tables 1 and 2.

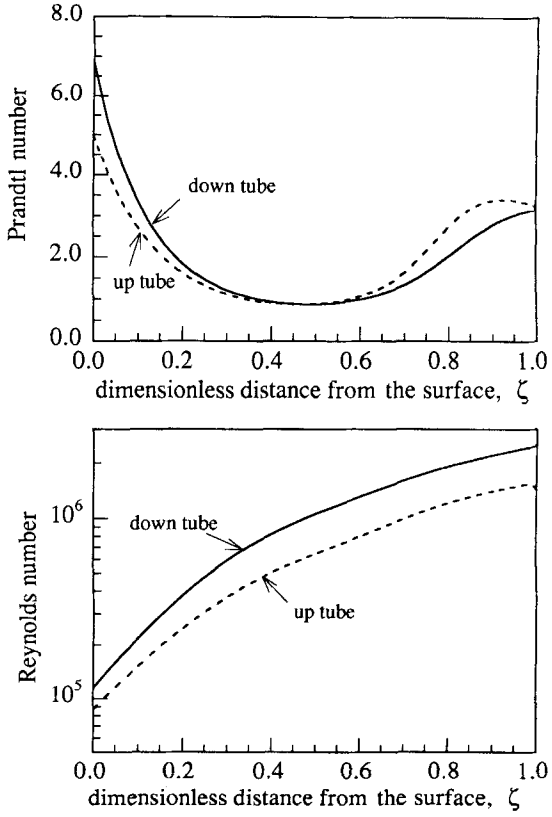

Figure 7. Variation of Prandtl and Reynolds number within the reactor for the ignited steady state of the base case.

Parameter values used to construct this figure are given in Tables 1 and 2.

here, we observed a sharp decrease in the values of the overall heat-transfer coefficient for the temperature slightly higher than that corresponding to the maximum specific heat. This sharp decrease is explained by already mentioned behavior of the specific heat C_p^*, as well as transition from liquid-like to gas-like values for the thermal conductivity of the reaction mixture in this region. This changes in the reaction mixture properties are reflected in the behavior of the Prandtl (Figure 7), as well as the Reynolds numbers in this region (Figure 7). Michna and Gloyna (1990) have experimentally observed a local maximum followed by a sudden decrease in the value of the heat-transfer coefficient in the transitional region. The reported values for the overall transfer coefficient agree with those obtained in our calculations.

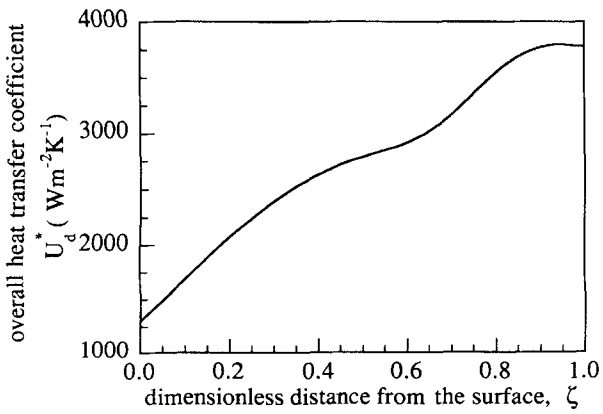

Figure 6. Variation of the overall heat-transfer coefficient U_d^* within the reactor for the ignited steady state of the base case.

Parameter values used to construct this figure are given in Tables 1 and 2.

Figure 4 shows that the temperature profile is almost flat near the bottom of the reactor. The temperature of the incoming reaction mixture increases only 30 K in the bottom quarter of the reactor. This is due to the sharp increase in the value of $\hat{C}_P$ in this region, as shown in Figure 8. On the other hand, the value of $\hat{C}_T$ decreases sharply in the bottom region of the reactor.

Figure 9 shows the effect of the Damköhler number (which is inversely proportional to the inlet flow rate) on the exit conversion and the bottom temperature. The base case corresponds to $Da = 2.807 \times 10^{-5}$, and economically interesting flow rates correspond to Da values smaller than 5.0×10^{-4}. These figures show that the reactor exhibits multiple steady state for all Damköhler numbers within the range of interest. This behavior is similar to that observed by Lovo et al. (1990). The maximum flow rate, however, is limited by hydrodynamical consideration rather than the oxidation kinetics. The maximum velocity ($\approx 4.0\ \mathrm{m \cdot s^{-1}}$) is limited by the overall pressure drop within the reactor, shown in Figure 10. (Here, the predictions of our model are not very accurate, since for very low pressures, one phase flow is not a reasonable assumption

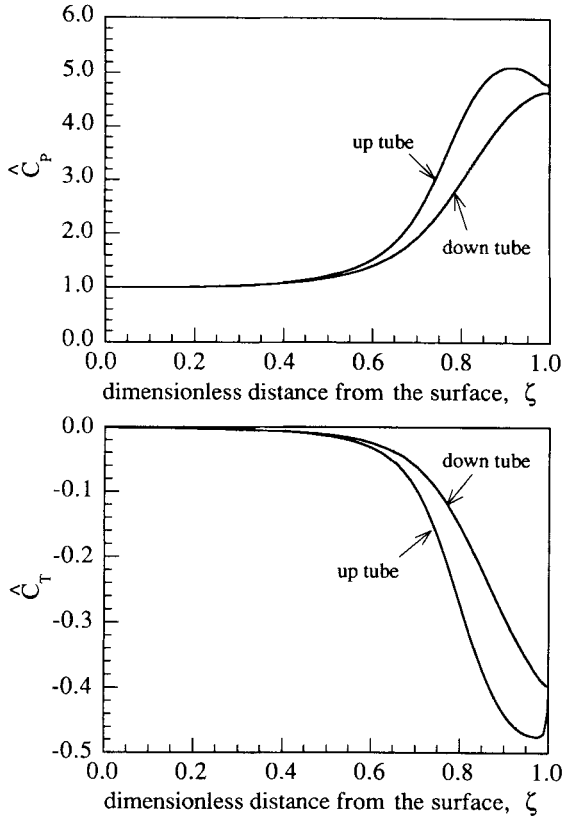

Figure 8. Variation of $\hat{C}_P$ and $\hat{C}_T$ within the reactor for the ignited steady state of the base case.

Parameter values used to construct this figure are given in Tables 1 and 2.

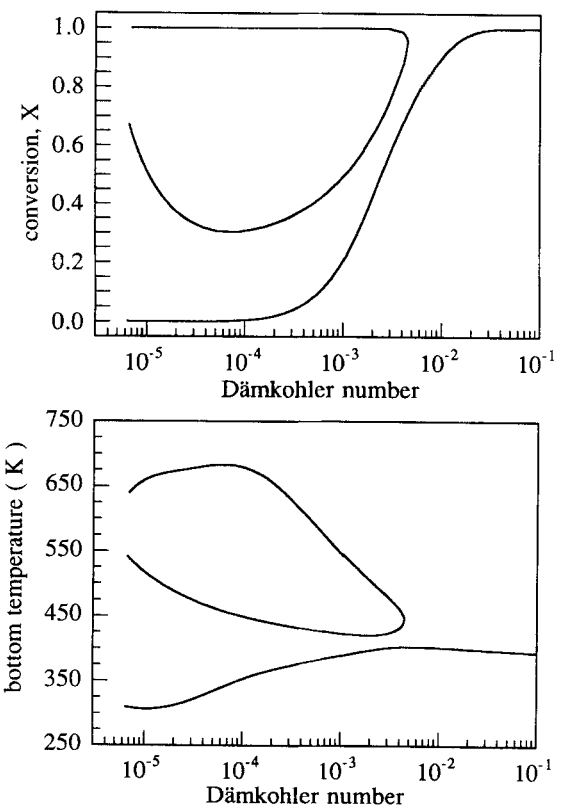

Figure 9. Bifurcation diagrams of conversion and bottom temperature vs. the Damköhler number (flow rate).

Parameter values used to construct this figure are: $T_o = 298.15$ K; $P_o^* = 100$ bar; $x_o = 0.01$; $L = 3{,}000$ m; $\zeta_m = 1.0$; $U_a^* = 2.0$ W·m^{-2}·K^{-1}.

any more.) In practice, the maximal pressure drop allowed in the reactor would be much lower. If, for instance, the maximal allowed pressure drop in the reactor is limited to 20% of the inlet pressure (up to 20 bar in this case), the maximum velocity that can be used is approximately 2.0 m·s^{-1}.

It is an interesting observation that for inlet velocities below 1.0 m·s^{-1} the outlet pressure is higher than the inlet pressure. For these inlet velocities, the friction loss is overbalanced by the buoyancy force due to the difference in the density of the reaction mixture in the down- and up-tubes (Figure 5).

Next, we examine the effect of the concentration of organics in the inlet stream on the conversion and the bottom temperature. Figure 11 shows that there exists a critical value of the organics concentration, below which only an extinguished steady state exists. Below this concentration the heat generated by the reaction is not sufficient for the reactor to operate autothermally. On the other hand, there exists an upper limit of the concentration of organics in the inlet stream that can be treated. For concentrations above this limit (≈ 2.0 wt. % of organics for stated conditions) the vaporization of the reaction mixture in the reactor occurs, as shown in Figure 12. Its top diagram shows the pressure and temperature profile (the reaction path) for the base case ($x_o = 0.01$) in the P-T diagram. The reaction path is well above the gas-liquid equilibrium curve, and the reaction mixture is either a subcritical liquid or a supercritical fluid. Shown in Figure 11, the bottom temperature on the ignited branch is almost independent of the organics concentration. The average temperature in the reactor, however, gets higher, as the concentration of organics in the feed increases. Higher temperature lowers the density of the reaction mixture that causes significant loss of the hydrostatic pressure and pushes the reaction pathway toward the gas-liquid equilibrium curve. The bottom diagram of Figure 12 shows the pathway for the case ($x_o \approx 0.02$), where the reaction pathway hits the gas-liquid equilibrium curve, which implies that within a certain region in the up-tube the reaction

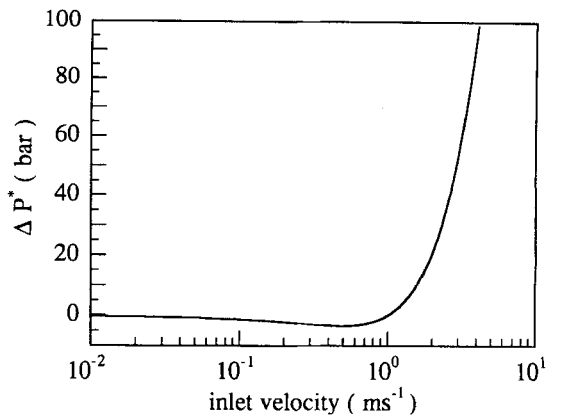

Figure 10. Pressure drop for the ignited steady state as a function of inlet velocity.

Parameter values used are the same as those used in constructing Figure 9.

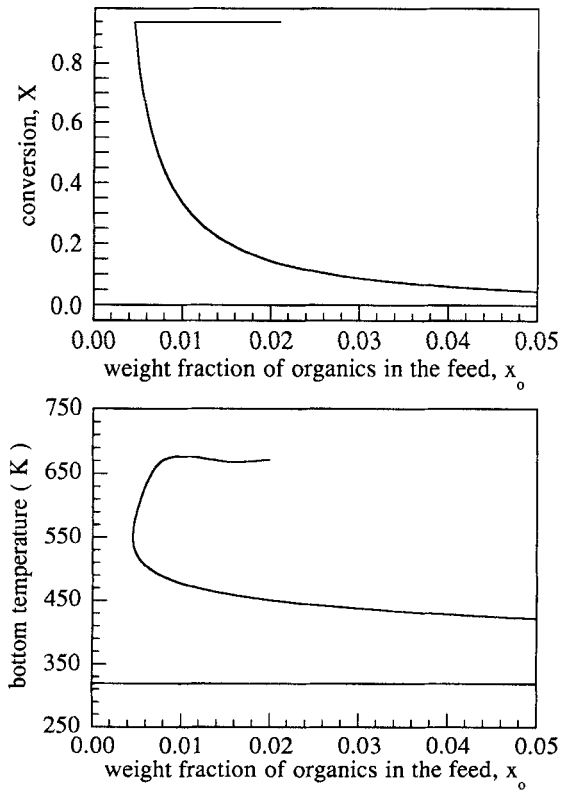

Figure 11. Bifurcation diagrams of conversion and bottom temperature vs. the inlet weight fraction of organics.

Parameter values used to construct this figure are: $T_o = 298.15$ K; $P_a^* = 100$ bar; $v_a^* = 1.0\ \mathrm{m \cdot s^{-1}}$, L = 3,000 m; $\zeta_{in} = 1.0$; $U_u^* = 2.0\ \mathrm{W \cdot m^{-2} \cdot K^{-1}}$.

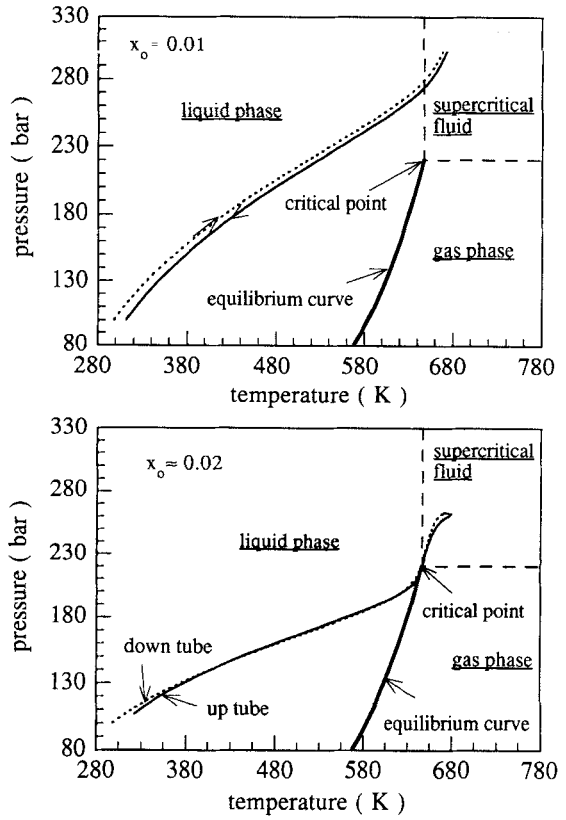

Figure 12. Reaction paths in the (P,T) plane of the ignited steady state for (a) base case, and (b) critical concentration of organics in the feed.

Parameter values used are the same as those used in constructing Figure 11.

mixture can become gaseous. (Note that our model breaks down if two-phase flow exists at any point in the reactor.) Such a situation should be avoided since this can cause instabilities in the reactor operation and cavitation that can seriously damage the reactor piping. This phenomenon imposes the upper limit on the feasible organics concentration. Higher concentrations, however, can be treated if the pressure at the bottom of the reactor is increased. One way to accomplish this is to cool the reaction mixture to increase its density and consequently increase the hydrostatic pressure head. In the EPA-sponsored full-scale plant in Longmont, Colorado, this was accomplished by the central heat exchanger (Rappe and Schwoyer, 1985).

To examine the effect of the additional heat removal on the reactor capacity, we vary the heat-transfer coefficient U_u^*. Figure 13 shows the effect of the concentration of organics in the feed on the exit conversion and the bottom temperature, respectively, for $U_u^* = 5.0\ \mathrm{W \cdot m^{-2} \cdot K^{-1}}$. Even with this higher heat loss to the rock, the bottom temperature (oxygen injection point) on the ignited branch is almost the same as before, and almost complete conversion is obtained on the ignited branch. However, the maximum concentration which can be treated is 25% higher ($x_o \approx 0.025$) than before. The minimum concentration of organics required for autothermal operation is higher too.

Figure 14 gives some additional insight into the effect of the additional heat removal on reactor performance. Although the exit conversion remains almost unaffected for large range of heat-transfer coefficient U_u^*, the bottom temperature on the ignited branch exhibits a maximum. For higher rates of heat removal ($U_u^* > 6.7\ \mathrm{W \cdot m^{-2} \cdot K^{-1}}$), it falls below the critical temperature. Figure 15 shows the effect of the additional heat removal on the bottom pressure. On the ignited branch, the bottom pressure is strongly affected, mostly through the effect of temperature on density of reaction stream and consequently on hydrostatic pressure head. The bottom pressure for $U_u^* = 5.0\ \mathrm{W \cdot m^{-2} \cdot K^{-1}}$ is 40 bar higher than that for the base case.

Figure 16 shows the effect of the reactor length on the exit conversion and the bottom temperature. The exit conversion on the ignited branch is unaffected for large variations in reactor length. The bottom temperature, however, falls below the critical value for $L < 1{,}900$ m. The reactor length is an extremely important design parameter of the deep-well process. Longer tubes provide higher hydrostatic pressure at the bottom of the reactor, larger area available for countercurrent heat exchange and longer residence time. Especially at higher flow rates, however, the pressure drop within such a long system may become significant.

Figure 17 shows the effect of different combinations of reactor length and inlet pressure on the bottom temperature. Other parameters used in the construction of this diagram are the same as those for the base case (see Tables 1 and 2). The diagram is divided into three regions:

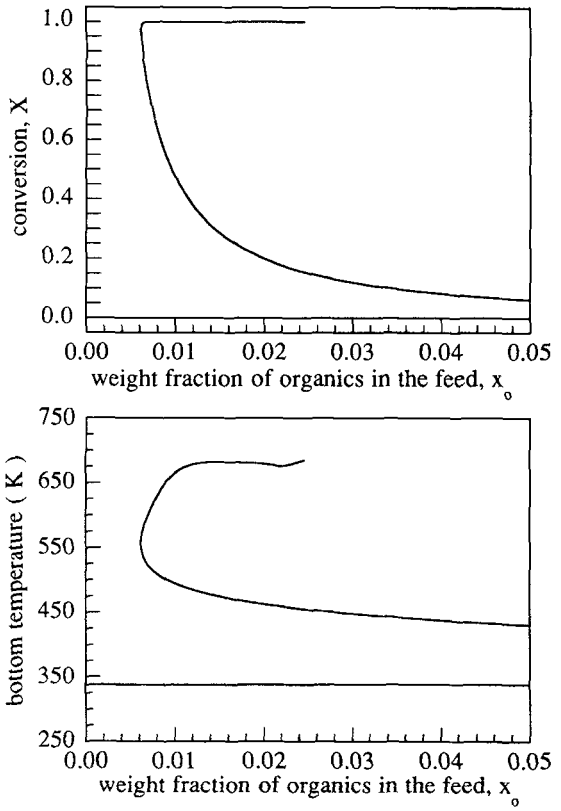

Figure 13. Bifurcation diagrams of conversion and bottom temperature vs. the inlet weight fraction of organics for increased heat removal.

Parameter values used to construct this figure are: $T_o = 298.15$ K; $P_o^* = 100$ bar; $v_o^* = 1.0\ \mathrm{m \cdot s^{-1}}$; $L = 3{,}000$ m; $\zeta_{in} = 1.0$; $U_u^* = 5.0\ \mathrm{W \cdot m^{-2} \cdot K^{-1}}$.

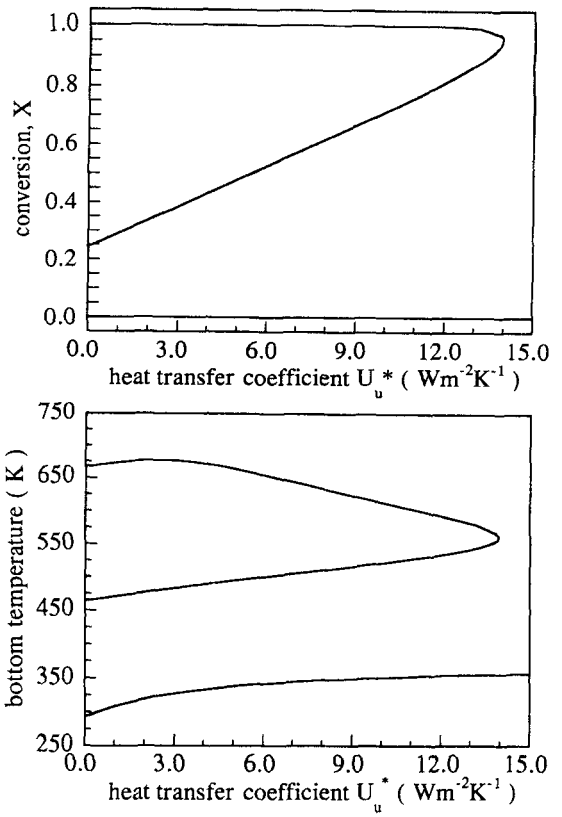

Figure 14. Bifurcation diagrams of conversion and bottom temperature vs. the heat removal from the reactor.

Parameter values used to construct this figure are: $T_o = 298.15$ K; $P_o^* = 100$ bar; $v_o^* = 1.0\ \mathrm{m \cdot s^{-1}}$; $x_o = 0.01$; $L = 3{,}000$ m; $\zeta_{in} = 1.0$.

(1) The region where operation should be avoided since vaporization of the reaction mixture is possible

(2) The region where operation is possible, but the temperature at the injection point of oxygen is below critical

(3) The region where supercritical operation is possible.

From the diagram it is clear that for supercritical operation with the bottom temperatures of at least 50 K above the critical temperature requires high bottom pressure. This can be obtained by either using a longer reactor or providing high inlet pressure or both. For higher flow rates and higher concentrations of organics, this diagram gets shifted toward higher inlet pressures and/or longer reactor lengths. As shown earlier, the additional heat removal (by using an internal heat exchanger) will increase the hydrostatic pressure at the bottom of the reactor, and therefore a shorter reactor and/or lower inlet pressures can be used.

As our model does not include the effect of reduced efficiency of the countercurrent heat exchange due to scale formation, tubes have to be a little longer than the calculated values to preheat the downcoming reaction mixture to supercritical conditions. This will shift the border between the subcritical and the supercritical operation in Figure 17 toward longer reactor lengths.

Figure 18 shows the effect of the oxygen injection depth on the exit conversion and the bottom temperature. For this case, the exit conversion on the ignited branch does not depend on the point where oxygen is injected. Injection in the lower 10% of the down-tube, however, is preferred, since the heat released by the reaction can be better utilized for preheating the downcoming reaction mixture. In addition, if oxygen is injected at the top, two-phase flow in the down-tube greatly reduces the hydrostatic head, and much longer reactor (or stronger pumps) will be required to reach the supercritical pressure near the bottom of the reactor. Figure 18 also shows that moving oxygen

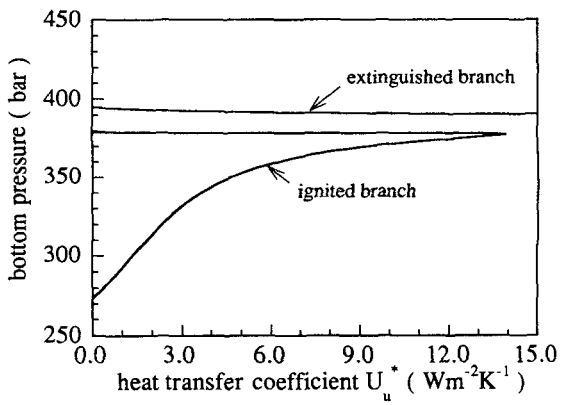

Figure 15. Effect of heat removal from the reactor on the bottom pressure.

Parameter values used are the same as those used in constructing Figure 14.

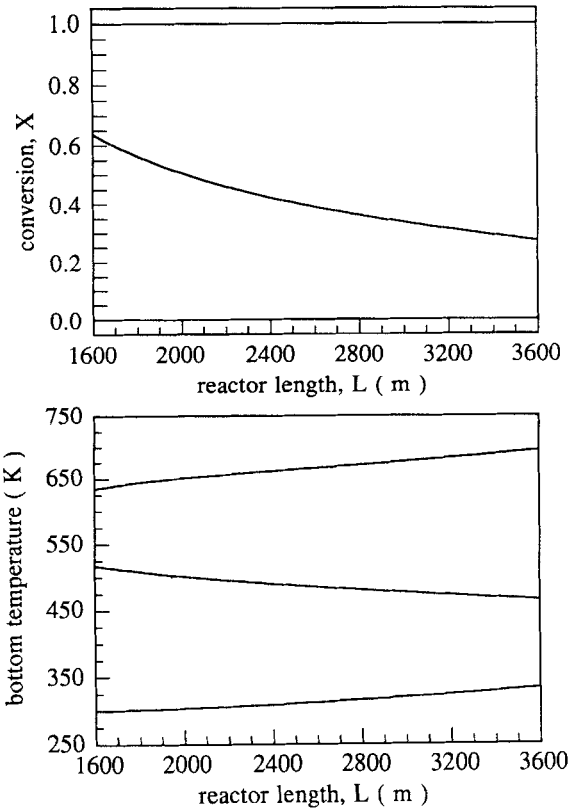

Figure 16. Bifurcation diagrams of conversion and bottom temperature vs. reactor length.

Parameter values used to construct this figure are: $T_o = 298.15$ K; $P_o^* = 100$ bar; $v_o^* = 1.0$ m·s^{-1}; $x_o = 0.01$; $\zeta_{in} = 1.0$; $U_u^* = 2.0$ W·m^{-2}·K^{-1}.

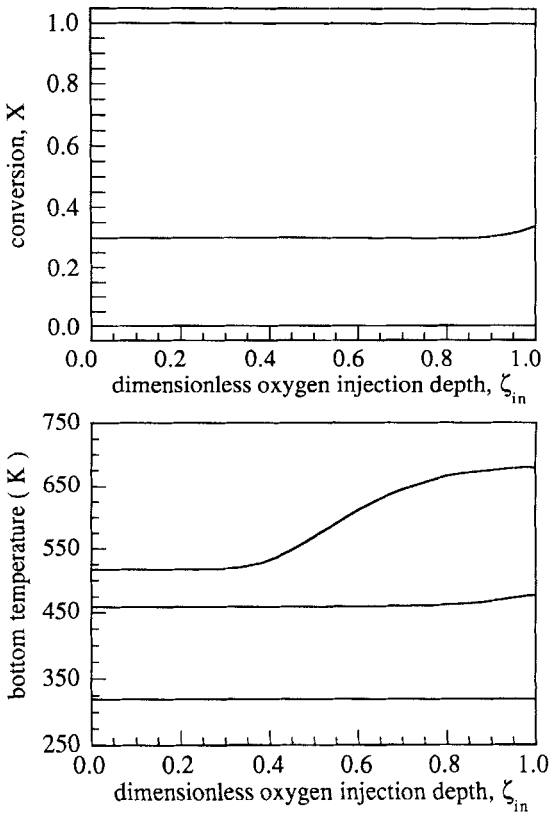

Figure 18. Bifurcation diagrams of conversion and bottom temperature vs. the oxygen injection depth.

Parameter values used to construct this figure are: $T_o = 298.15$ K; $P_o^* = 100$ bar; $v_o^* = 1.0$ m·s^{-1}; $x_o = 0.01$; $L = 3{,}000$ m; $U_u^* = 2.0$ W·m^{-2}·K^{-1}.

injection depth toward surface decreases the bottom temperature. In fact, the average temperature in the reactor decreases, as more and more energy released by the reaction is washed out with the effluent without being utilized for preheating of incoming reaction mixture. If oxygen is injected above a certain point, the temperature everywhere in the reactor falls below

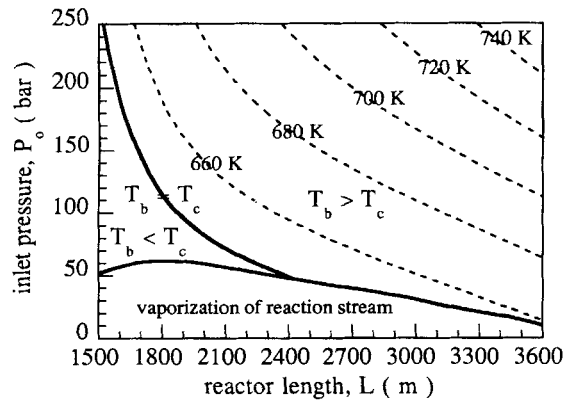

Figure 17. Effect of inlet pressure and reactor length on the bottom temperature.

Parameter values used to construct this figure are: $T_o = 298.15$ K; $v_o^* = 1.0$ m·s^{-1}; $x_o = 0.01$; $L = 3{,}000$ m; $\zeta_{in} = 1.0$; $U_u^* = 2.0$ W·m^{-2}·K^{-1}.

critical temperature. In this region, one-phase flow is not a reasonable assumption, and results obtained by our model are not reliable any more.

Finally, Figure 19 shows the effect of the feed temperature on the exit conversion and the bottom temperature. The exit conversion on the ignited branch is independent of the inlet temperature. Again, the highest feed temperature is limited by the possibility of the vaporization of the reaction mixture. The limit, however, is above the temperature range of interest.

Conclusions

We have developed a mathematical model that describes the qualitative behavior of the deep-well oxidation reactor for operation under supercritical conditions. Numerical simulations of the model have shown that the reactor exhibits multiple steady states for practical range of operating conditions. The maximum inlet velocity and the maximum concentration of organics are limited by hydrodynamical consideration, rather than by the oxidation kinetics. The same is found to be true for the maximum feed temperature, although here the upper limit is out of the practical range of interest.

Higher flow rates or higher concentrations of organics require high pressures at the bottom of the reactor that requires high inlet pressure and/or a very long reactor. Using an internal

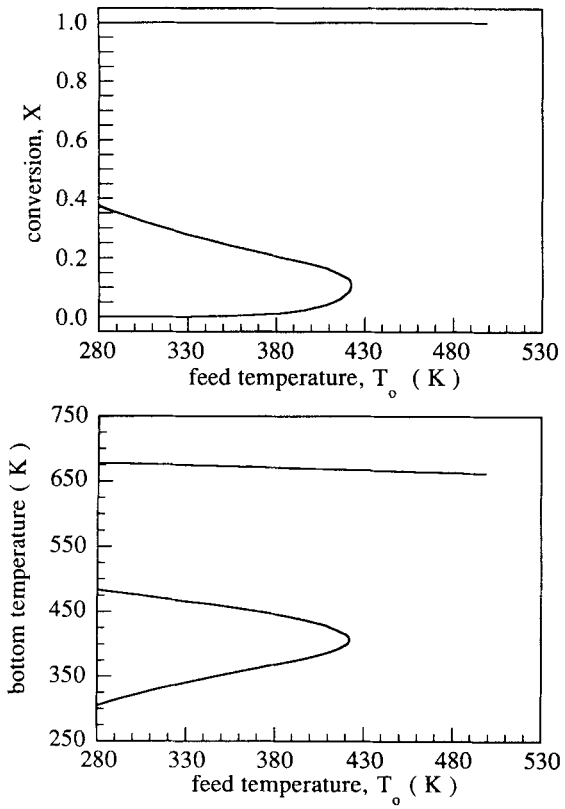

Figure 19. Bifurcation diagrams of conversion and bottom temperature vs. inlet temperature.

Parameter values used to construct this figure are: $P_o^* = 100$ bar; $v_o^* = 1.0\ \mathrm{m \cdot s^{-1}}$; $x_o = 0.01$; $L = 3{,}000$ m; $\zeta_{in} = 1.0$; $U_a^* = 2.0\ \mathrm{W \cdot m^{-2} \cdot K^{-1}}$; $E_{act}/R = 8{,}944.5$ K.

heat exchanger, which removes excessive heat from the reaction mixture, can greatly improve the reactor performance allowing treatment of higher flow rates and higher concentrations of organics. The calculations also show that there exists a lower limit of organics concentration, below which autothermal operation of the reactor is not possible.

The quantitative predictions of the present model can be greatly improved by obtaining more reliable kinetic data. In addition, more data on the solubility of gases (O_2, N_2, CO_2) within the range of temperatures and pressures are needed to model two-phase flow that may occur in the subcritical region of the reactor. This will be pursued in future work.

In this work, we have not addressed the stability of the steady states. It is well known that for the case of autothermal reactors, where three steady-state solutions exist, the ignited and extinguished steady states are stable, while the middle steady state is unstable. The unstable state provides information on the initial (startup) conditions leading to the ignited steady state.

The model developed here may also be used to study the transient behavior of the supercritical deep-well oxidation reactor.

Acknowledgment

This work is supported by the Gulf Coast Hazardous Substance Research Center and the Robert A. Welch Foundation.

Notation

a = ratio of cross-sectional areas of up- and down-tubes (A_u/A_d)
$\underline{A}$ = Helmholtz function, specific Helmholtz energy, $\mathrm{J \cdot kg^{-1}}$
A = cross-sectional area of a tube, $\mathrm{m^2}$
b = modified length to diameter ratio
C_p^* = specific heat at constant pressure, $\mathrm{J \cdot kg^{-1} \cdot K^{-1}}$
C_v^* = specific heat at constant volume, $\mathrm{J \cdot kg^{-1} \cdot K^{-1}}$
$\hat{C}_P^*$ = partial derivative of internal energy with respect to temperature at constant pressure, $\mathrm{J \cdot kg^{-1} \cdot K^{-1}}$
$\hat{C}_P$ = dimensionless partial derivative of internal energy with respect to temperature at constant pressure
$\hat{C}_T^*$ = partial derivative of internal energy with respect to pressure at constant temperature, $\mathrm{J \cdot kg^{-1} \cdot Pa^{-1}}$
$\hat{C}_T$ = dimensionless partial derivative of internal energy with respect to pressure at constant temperature
D = tube diameter, m
Da = Damköhler number
e = roughness of the tube, m
E_{act} = activation energy, $\mathrm{J \cdot mol^{-1}}$
Eu = Euler number
f = friction factor
g = acceleration due to gravity = $9.81\ \mathrm{m \cdot s^{-2}}$
$\underline{H}$ = specific enthalpy, $\mathrm{J \cdot kg^{-1}}$
$(-\Delta\underline{H}_r)$ = heat of reaction, $\mathrm{J \cdot kg^{-1}}$
H = Heaviside's function
$\hat{H}$ = function defined by Eq. 5
k_o = preexponential factor, $\mathrm{s^{-1}}$
L = length of the reactor, m
M = molecular weight, $\mathrm{kmol^{-1}}$
Nu = Nusselt number
p = perimeter of the tube, m
P = dimensionless pressure
P^* = pressure, Pa
Pr = Prandtl number
q = heat flux, $\mathrm{W \cdot m^{-2}}$
Q_{loss} = heat losses from the up-tube to the surrounding earth, $\mathrm{W \cdot m^{-1}}$
r = radial coordinate
R = universal gas constant, $\mathrm{J \cdot mol^{-1} \cdot K^{-1}}$
R_h = hydraulic radius, m
R_u = radius of the up-tube, m
Re = Reynolds number
Ri = Richardson number
St = Stanton number
t = time, s
T = absolute temperature, K
U = dimensionless heat-transfer coefficient
U^* = heat-transfer coefficient, $\mathrm{W \cdot m^{-2} \cdot K^{-1}}$
$\underline{U}$ = specific internal energy, $\mathrm{J \cdot kg^{-1}}$
v = dimensionless velocity
v^* = velocity, $\mathrm{m \cdot s^{-1}}$
x = mass fraction
X = dimensionless concentration or steady-state conversion
y = dimensionless temperature
z = axial coordinate, m

Greek letters

α = geothermal temperature gradient = $0.029\ \mathrm{km^{-1}}$
α_e = thermal diffusivity of the earth, $\mathrm{m^2 \cdot s^{-1}}$
β = adiabatic temperature rise for constant properties model
ϵ = dimensionless heat capacity of reactor piping
γ = dimensionless activation energy
λ = thermal conductivity, $\mathrm{W \cdot m^{-1} \cdot K^{-1}}$
ρ^* = density, $\mathrm{kg \cdot m^{-3}}$
ρ = dimensionless density
τ = dimensionless time
Ω = dimensionless group, ratio of pressure energy to internal energy
ζ = dimensionless axial coordinate

Subscripts and superscripts

a = ambient

d = down
e = earth
f = front
in = oxygen injection point
o = inlet
m = metal, reactor piping
u = up

Literature Cited

Carslaw, H. S., and J. C. Jaeger, *Conduction of Heat in Solids*, 2nd ed., Clarendon Press, Oxford (1989).

Haaland, S. E., "Simple and Explicit Formulas for the Friction Factor in Turbulent Pipe Flow," *J. of Fluids Eng.*, **105**, 89 (1983).

Haar, L., J. S. Gallagher, and G. S. Kell, *NBS/NRC Steam Tables*, Hemisphere Publishing Corp., New York (1984).

Helling, R. K., and J. W. Tester, "Oxidation Kinetics of Carbon Monoxide in Supercritical Water," *Energy & Fuels*, **1**(5), 417 (1987).

Helling, R. K., and J. W. Tester, "Oxidation of Simple Compounds and Mixtures in Supercritical Water: Carbon Monoxide, Ammonia, and Ethanol," *Environ. Sci. Technol.*, **22**(11), 1319 (1988).

Josephson, J., "Supercritical Fluids," *Environ. Sci. Technol.*, **16**(10), 548A (1982).

Kaufmann, L. A., and H. Peterscheck, "Modeling Vertech's Mile-Long Multiphase Reaction Vessel," *Chem. Eng. Sci.*, **41**(4), 685 (1986).

Lovo, M., H. A. Deans, and V. Balakotaiah, "Modeling and Simulation of Aqueous Hazardous Waste Oxidation in Deep-Well Reactors," *Chem. Eng. Sci.*, **45**(8), 2703 (1990).

Lovo, M., and V. Balakotaiah, "Multiplicity Features of Adiabatic Autothermal Reactors," *AIChE J.*, **38**(1), 101 (1992a).

Lovo, M., and V. Balakotaiah, "Multiplicity Features of Nonadiabatic, Tubular Autothermal Reactors," *AIChE J.*, **38**(1), 116 (1992b).

Michna, R. J., and E. F. Gloyna, "Heat Transfer to Water in Countercurrent Flow within a Vertical, Concentric-Tube Supercritical Water Oxidation Reactor," Center for Research in Water Resources, Univ. of Texas at Austin, Technical Report CRWR 195 (1990).

Mittal, S., H. A. Deans, and T. E. Tezduyar, "Numerical Simulation of Deep-Well Wet-Oxidation Reactor using Steam," *J. of Eng. Mechanics*, **117**, 798 (1991).

Modell, M., G. G. Gaudet, M. Simson, G. T. Hong, and K. Biemann, "Supercritical Water," *Solid Wastes Management*, **25**(8), 26 (1982).

Monrad, C. C., and J. F. Pelton, "Heat Transfer by Convection in Annular Spaces," *Trans. Amer. Inst. Chem. Eng.*, **38**, 593 (1942).

Rappe, G. C., and W. L. Schwoyer, "Mile-Deep Reactor Destroys Sludge with Ease," *Water Engineering & Management*, **130**(10), 27 (1985).

Shanableh, A., and E. F. Gloyna, "Supercritical Water Oxidation—Wastewaters and Sludges," *Wat. Sci. Tech.*, **23**, 389 (1991).

Smith, J. M., and T. J. Raptis, "Supercritical Deep-Well Wet Oxidation of Liquid Organic Wastes," *Int. Symp. on Subsurface Injection of Liquid Wastes* (Mar., 1986).

Tezduyar, T., J. Marble, and H. A. Deans, "Finite Element/Finite Difference Analysis of a Deep-Well Oxidation Process," *Numerical Methods in Thermal Problems*, Vol. V, Part 2, Proc. Int. Conf., Montreal, Canada (1987).

Thomason, T. B., and M. Modell, "Supercritical-Water Destruction of Aqueous Wastes," *Hazardous Waste*, **1**(4), 453 (1984).

Yang, H. H., and C. A. Eckert, "Homogeneous Catalysis in the Oxidation of *p*-Chlorophenol in Supercritical Water," *Ind. Eng. Chem. Res.*, **27**(11), 2009 (1988).

Appendix A: Derivation of Energy Balances

Neglecting kinetic and potential energy, as well as any heat conduction in a tube, the unsteady-state energy balances for the down-tube can be written as:

$$A_{md}\rho_m^*\frac{\partial \underline{U}_{md}}{\partial t}+A_d\frac{\partial(\rho_d^*\underline{U}_d)}{\partial t}+A_d\frac{\partial(\rho_d^* v_d^*\underline{H}_d)}{\partial z}-p_d U_d^*(T_u-T_d)=0 \quad \text{(A1)}$$

Writing

$$\underline{H}_d=\underline{U}_d+P_d^*\underline{V}_d=\underline{U}_d+P_d^*/\rho_d^* \quad \text{(A2)}$$

and combining with the unsteady-state continuity equation (Eq. 6), Eq. A1 becomes:

$$A_{md}\rho_m^*\frac{\partial \underline{U}_{md}}{\partial t}+A_d\rho_d^*\frac{\partial \underline{U}_d}{\partial t}+A_d\rho_d^* v_d^*\frac{\partial \underline{U}_d}{\partial z}+A_d\frac{\partial(P_d^* v_d^*)}{\partial z}-p_d U_d^*(T_u-T_d)=0 \quad \text{(A3)}$$

Assuming that the reaction mixture behaves as an ideal solution:

$$\underline{U}_d=\sum_{i=1}^{s}x_{id}\underline{U}_{id} \quad \text{(A4)}$$

where the summation is over all the species present in the stream.

Using Eq. A4, Eq. A3 can be written in the following form:

$$A_{md}\rho_m^*\frac{\partial \underline{U}_{md}}{\partial t}+A_d\rho_d^*\left\{\sum_{i=1}^{s}x_{id}\frac{\partial \underline{U}_{id}}{\partial t}+\sum_{i=1}^{s}\frac{\partial x_{id}}{\partial t}\underline{U}_{id}\right\}+A_d\rho_d^* v_d^*\left\{\sum_{i=1}^{s}x_{id}\frac{\partial \underline{U}_{id}}{\partial z}+\sum_{i=1}^{s}\frac{\partial x_{id}}{\partial z}\underline{U}_{id}\right\}+A_d\frac{\partial(P_d^* v_d^*)}{\partial z}-p_d U_d^*(T_u-T_d)=0 \quad \text{(A5)}$$

The terms:

$$A_d\rho_d^*\sum_{i=1}^{s}\underline{U}_{id}\left[\frac{\partial x_{id}}{\partial t}+v_d^*\frac{\partial x_{id}}{\partial z}\right] \quad \text{(A6)}$$

can be combined with the species balances for all species in the reaction mixture, which can be, using assumed lumped reaction $A+\nu B\rightarrow P$, written as:

$$\frac{\partial x_{id}}{\partial t}+v_d^*\frac{\partial x_{id}}{\partial z}-k_o\exp\left(-\frac{E_{act}}{RT_d}\right)x_{Ad}\nu_i\frac{M_i}{M_A}H(z-z_{in})\hat{H}_d=0 \quad \text{(A7)}$$

In the equation above, A represents organic component, and ν_i's are stoichiometric coefficients for various species. Thus, Eq. A6 becomes:

$$A_d\rho_d^* k_o\exp\left(-\frac{E_{act}}{RT_d}\right)\frac{x_{Ad}}{M_A}H(z-z_{in})\hat{H}_d\sum_{i=1}^{s}\underline{U}_{id}\nu_i M_i=A_d\rho_d^* k_o\exp\left(-\frac{E_{act}}{RT_d}\right)\frac{x_{Ad}}{M_A}H(z-z_{in})\hat{H}_d\Delta U_r \quad \text{(A8)}$$

The quantity ΔU_r represents the change in internal energy due to reaction at constant volume per mole of A reacted. Dividing ΔU_r by M_A gives heat released per unit mass of A

reacted. For condensed-phase systems, $\Delta U_r \approx \Delta H_r$. With this approximation, Eq. A5 becomes:

$$A_{md}\rho_m^* \frac{\partial \underline{U}_{md}}{\partial t} + A_d\rho_d^* \sum_{i=1}^{s} x_{id} \frac{\partial \underline{U}_{id}}{\partial t} + A_d\rho_d^* v_d^* \sum_{i=1}^{s} x_{id} \frac{\partial \underline{U}_{id}}{\partial z} + A_d \frac{\partial (P_d^* v_d^*)}{\partial z} - A_d\rho_d^* k_o \exp\left(-\frac{E_{act}}{RT_d}\right) x_{Ad} H(z - z_{in}) \hat{H}_d(-\Delta \underline{H}_r) - p_d U_d^* (T_u - T_d) = 0 \quad \text{(A9)}$$

Since water is the major component of the reaction mixture, we assume that the properties of the reaction mixture can be approximated by the properties of pure water. Thus, the second and third terms in Eq. A9 can be replaced by:

$$A_d\rho_d^* \frac{\partial \underline{U}_{wd}}{\partial t} + A_d\rho_d^* v_d^* \frac{\partial \underline{U}_{wd}}{\partial z} \quad \text{(A10)}$$

where subscript w stands for water. Dropping this subscript, Eq. A9 becomes:

$$A_{md}\rho_m^* \frac{\partial \underline{U}_{md}}{\partial t} + A_d\rho_d^* \frac{\partial \underline{U}_d}{\partial t} + A_d\rho_d^* v_d^* \frac{\partial \underline{U}_d}{\partial z} + A_d \frac{\partial (P_d^* v_d^*)}{\partial z} - A_d(-\Delta \underline{H}_r) k_o \exp\left(-\frac{E_{act}}{RT_d}\right) x_d\rho_d^* H(z - z_{in}) \hat{H}_d - p_d U_d^* (T_u - T_d) = 0 \quad \text{(A11)}$$

Here, $\underline{U}_d$ and ρ_d^* are the internal energy per unit mass and the density of pure water at P_d^* and T_d, respectively. We have also dropped the subscript A on x_{Ad}.

Expanding $\underline{U}_{md}$ and $\underline{U}_d$, we obtain:

$$A_{md}\rho_m^* C_{vm}^* \frac{\partial T_d}{\partial t} + A_d\rho_d^* \left[\frac{\partial \underline{U}_d}{\partial T_d}\frac{\partial T_d}{\partial t} + \frac{\partial \underline{U}_d}{\partial P_d^*}\frac{\partial P_d^*}{\partial t}\right] + A_d\rho_d^* v_d^* \left[\frac{\partial \underline{U}_d}{\partial T_d}\frac{\partial T_d}{\partial z} + \frac{\partial \underline{U}_d}{\partial P_d^*}\frac{\partial P_d^*}{\partial z}\right] + A_d \frac{\partial (P_d^* v_d^*)}{\partial z} - A_d(-\Delta \underline{H}_r) k_o \exp\left(-\frac{E_{act}}{RT_d}\right) x_d\rho_d^* H(z - z_{in}) \hat{H}_d - p_d U_d^* (T_u - T_d) = 0 \quad \text{(A12)}$$

The partial derivatives of internal energy with respect to temperature and pressure can be written as:

$$\frac{\partial \underline{U}}{\partial T} = \frac{\partial \underline{H}}{\partial T} + \frac{P^*}{\rho^{*2}}\frac{\partial \rho^*}{\partial T} = C_p^* + \frac{P^*}{\rho^{*2}}\frac{\partial \rho^*}{\partial T} \quad \text{(A13)}$$

$$\frac{\partial \underline{U}}{\partial P^*} = \frac{\partial \underline{H}}{\partial P^*} - \frac{1}{\rho^*} + \frac{P^*}{\rho^{*2}}\frac{\partial \rho^*}{\partial P^*} = \frac{1}{\rho^*} + \frac{T}{\rho^{*2}}\frac{\partial \rho^*}{\partial T}$$

$$-\frac{1}{\rho^*} + \frac{P^*}{\rho^{*2}}\frac{\partial \rho^*}{\partial P^*} = \frac{1}{\rho^{*2}}\left(T\frac{\partial \rho^*}{\partial T} + P^*\frac{\partial \rho^*}{\partial P^*}\right) \quad \text{(A14)}$$

We denote these two partial derivatives by $\hat{C}_P^*$ and $\hat{C}_T^*$, respectively. Substitution into Eq. A12 gives Eq. 3. The energy balance for the up-tube (Eq. 4) can be obtained in a similar way.

Appendix B: Temperature Distribution in the Surrounding Earth

Estimation of the heat losses from the up-tube to the surrounding earth can be obtained by solving the unsteady-state conduction equation for the surrounding earth:

$$\rho_e^* C_e^* \frac{\partial T_e}{\partial t} = \lambda_e \left\{\frac{1}{r}\frac{\partial}{\partial r}\left(r\frac{\partial T_e}{\partial r}\right) + \frac{\partial^2 T_e}{\partial z^2}\right\} \quad \text{(B1)}$$

Initial conditions are as follows:

$$t = 0 \quad T_e = T_a + \alpha z \qquad r > R_u \qquad 0 < z < L \quad \text{(B2)}$$

$$T_e = T_a + \alpha z \qquad r > 0 \qquad z > L \quad \text{(B3)}$$

where α is the geothermal temperature gradient in the earth.

The boundary conditions are given by:

$$t > 0 \quad T_e = T_u(t,z) \qquad r = R_u \qquad 0 < z < L \quad \text{(B4)}$$

$$T_e = T_u(t,L) \qquad 0 < r < R_u \qquad z = L \quad \text{(B5)}$$

$$\frac{\partial T_e}{\partial r} = 0 \qquad r = 0 \qquad L < z < L_p \quad \text{(B6)}$$

$$-\lambda_e \frac{\partial T_e}{\partial z} = U_a^*(T_a - T_e) \qquad r > R_u \qquad z = 0 \quad \text{(B7)}$$

Far away from the reactor, the influence of the reactor on the earth temperature is negligible and we can write:

$$t > 0 \quad T_e = T_a + \alpha z \qquad r = R_p \qquad \forall z \quad \text{(B8)}$$

$$T_e = T_a + \alpha L_p \qquad \forall r \qquad z = L_p \quad \text{(B9)}$$

where R_p and L_p are the heat penetration depths in the radial and axial direction, respectively. These are selected so that the influence of the reactor on the earth's temperature profile can be neglected. Equations B1-B9 must be solved numerically. An analytical solution, however, exists for the flux at the surface of an infinite cylinder of radius R_u kept at constant surface temperature T_s, immersed in an infinite medium at temperature T_a. The flux at time t is given in the form of an integral (Carslaw and Jaeger, 1989):

$$q = \frac{4(T_s - T_a)\lambda_e}{\pi^2 R_u} \int_0^\infty \frac{\exp(-\alpha_e u^2 t)du}{u[J_o^2(R_u u) + Y_o^2(R_u u)]} \quad \text{(B10)}$$

Equation B10 implies that the surface flux is proportional to temperature difference between the surface and the medium and the surface flux can be estimated by an expression similar to Eq. 14 with a heat-transfer coefficient that varies with time.

It follows from Eq. B10 that the effective heat-transfer coefficient is given by:

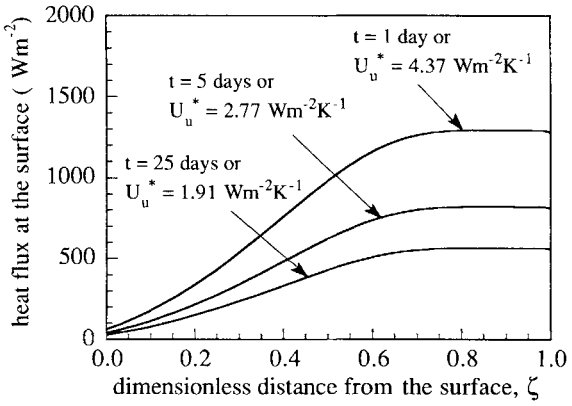

Figure B1. Heat losses from the up-tube of the reactor obtained by solving the unsteady-state heat equation for surrounding earth and estimated by treating the surrounding earth as an infinite heat reservoir.

$$U_u^* = \frac{4\lambda_e}{\pi^2 R_u} \int_0^\infty \frac{\exp(-\phi\xi^2)d\xi}{\xi[J_o^2(\xi) + Y_o^2(\xi)]} \qquad \text{(B11)}$$

where $\phi = \alpha_e t / R_u^2$.

For short times ($\phi \ll 1$), Eq. B11 simplifies to (Carslaw and Jaeger, 1989):

$$U_u^* = \frac{\lambda_e}{R_u}\left\{(\pi\phi)^{-0.5} + \frac{1}{2} - \frac{1}{4}(\phi/\pi)^{0.5} + \ldots.\right\} \qquad \text{(B12)}$$

while for very long times ($\phi \gg 1$), it simplifies to (Carslaw and Jaeger, 1989):

$$U_u^* = \frac{2\lambda_e}{R_u}\left\{\frac{1}{\ln(4\phi) - 2\gamma} - \frac{\gamma}{[\ln(4\phi) - 2\gamma]^2} - \ldots..\right\} \qquad \text{(B13)}$$

where $\gamma = 0.57722...$ is the Euler's constant.

The solutions given by Eqs. B10–B13 are not directly applicable to our case as the temperature of the earth varies linearly with depth and the surface temperature of the down-tube is not constant. We solved Eqs. B1–B9 numerically using a finite difference method with nonequidistant grid mesh for various steady-state temperature profiles in the up-tube obtained by solving the reactor model equations. The values of thermal conductivity and thermal diffusivity of the earth used in these calculations were 0.52 W·m^{-1}·K^{-1} and 0.144×10^{-6} m^2·s^{-1}, respectively, and were assumed constant. Figure B1 shows heat fluxes from surface of the reactor calculated by solving Eqs. B1–B9, with $R_p = 1{,}000 \times R_u$ (= 152.0 m) and $L_p = 0.001 \times L$ (= 3.0 m) and the heat flux calculated by Eq. 14. (The two curves are indistinguishable on the scale used in Figure B1.) In both cases, the surface temperature is taken to be the profile in Figure 4. It follows from this comparison that by adjusting the value for U_u^*, one can easily estimate the heat losses from the reactor at any time.

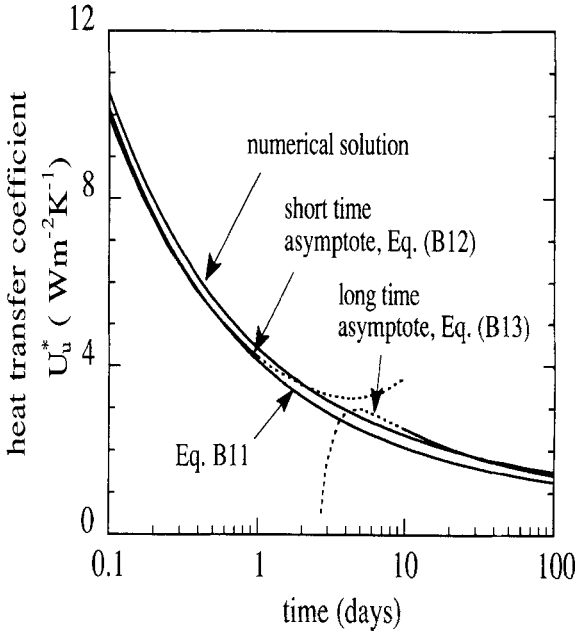

Figure B2. Effective heat-transfer coefficient U_u^* vs. time.

Figure B2 gives the value for the effective heat-transfer coefficient U_u^* in Eq. 14, which gives the same heat flux at the surface of the reactor as that obtained by numerical solution of Eqs. B1–B9. This figure also compares our numerical solution to the analytical solution for an infinite cylinder with constant and uniform surface temperature given by Eq. B11. The solutions valid for short and long times (Eqs. B12 and B13, respectively) are also shown. The figure shows that, in both cases, the value for U_u^* is inversely proportional to square root of time for short times ($\phi < 1$). For times longer than 1 day ($1 < \phi < 100$), our numerical solution can be fitted by the following expression:

$$\mathrm{Nu} = 0.079\ \phi^{-0.23} \qquad \text{(B13)}$$

where

$$\mathrm{Nu} = \frac{U_u^* R_u}{\lambda_e}.$$

After approximately 20 days, the value of U_u^* falls to 2.0 W·m^{-2}·K^{-1}. This value has been chosen as a base case value of the heat-transfer coefficient U_u^* used in our steady-state computations.

Manuscript received Oct. 25, 1991, and revision received Mar. 27, 1992.